Solid Freeform Fabrication 2021: Proceedings of the 32nd Annual International
Solid Freeform Fabrication Symposium – An Additive Manufacturing Conference
Reviewed Paper

A Comparative Study on the Microstructure and Texture Evolution of L-PBF and LP-DED 17-4 PH Stainless Steel during Heat Treatment

P.D. Nezhadfar[1,2], Paul R. Gradl[3], Shuai Shao[1,2], Nima Shamsaei[1,2]

[1]Department of Mechanical Engineering, Auburn University, Auburn, AL, USA
[2]National Center for Additive Manufacturing Excellence (NCAME), Auburn University, Auburn, AL, USA

[3] NASA Marshall Space Flight Center, Propulsion Department, Huntsville, AL 35812, USA

[*]Corresponding author:
Email: shamsaei@auburn.edu
Phone: (334) 844 4839

Abstract

This study aims to characterize the microstructure and crystallographic texture of 17-4 PH stainless steel (SS) manufactured with laser powder directed energy deposition (LP-DED) and laser powder bed fusion (L-PBF), in both non-heat treated and heat treated conditions. It is found that the non-heat treated LP-DED 17-4 PH SS possesses coarse columnar ferrite grains decorated with Widmanstätten ferrite grains, whereas the L-PBF counterpart has very fine and mostly equiaxed ferrite grains along with lath martensite. An identical stress relief (SR) temperature is obtained for both the L-PBF and LP-DED 17-4 PH SS samples based on the phase diagrams generated using Thermo-Calc. software. The SR step prior to CA-H1025 heat treatment resulted in texture weakening and slightly refined the grain structure. The non-heat treated L-PBF 17-4 PH SS sample possesses strong cube and γ-fiber textures, while the texture transfers to weaker γ-fiber components after performing SR-CA-H1025 heat treatment.

Keywords: Laser powder directed energy deposition (LP-DED); Laser powder bed fusion (L-PBF); Stainless steel; Microstructure; Texture

A substantially improved version of this paper appears in a special issue of the TMS publication *JOM*, March 2022.

Introduction

Additive manufacturing (AM), a family of layer-by-layer digital manufacturing processes, delivers ample opportunities for fabricating near-net-shape or final shape parts with complex internal and external geometries, high freedom in the design, manufacture of customized parts on demand, and consequently have drawn much attention from various industrial sectors [1]. Among all the AM methods, the laser-based methods, i.e., laser powder bed fusion (L-PBF), and laser powder directed energy deposition (LP-DED) are the most widely used ones [2]. In the L-PBF process, there is a powder bed in which a re-coater provides a new layer of powder with each pass and the powder particles are melted locally in a defined pattern by a (few) high-energy laser source(s) and fused to the previously fused layers. In the LP-DED process, the powder is blown to the melt pool, and a new layer of material is fabricated. The L-PBF process is typically limited to a single-powder feedstock; however, provides more freedom in the design of near-net-shaped parts with higher geometrical resolution than the LP-DED process [3]. Conversely, LP-DED is suitable for multi-powder feedstock, functionally graded components, and the fabrication of large parts since there is no restriction of the build box [4].

It has been shown that the AM materials regardless of the manufacturing technique (e.g., L-PBF or LP-DED) exhibit comparable, and in some cases superior/inferior, static mechanical properties as compared to the conventionally manufactured (CM) counterparts [5,6]. This is ascribed to the rapid cooling/solidification rate of AM processes leading to a finer microstructure in AM materials as compared to that of the CM ones, such as casting. Nevertheless, the AM materials experience high melting and cooling/solidification rates, which results in the formation of defects such as pores, lack of fusion (LoF) defects, and inclusions, high surface roughness, and residual stress, all of which affect their fatigue resistance [7,8]. In addition, it has been reported that there is a significant variation in the cooling/solidification rate of L-PBF and LP-DED methods; L-PBF results in three orders of magnitude higher cooling rate than LP-DED [3]. This causes variation in the thermal history a part experiences during fabrication via each of these AM processes, which results in different micro-/defect- structure, and consequently, differences in the mechanical properties.

Babuska et al. [3] has recently compared the microstructure and mechanical properties of CoCr alloy manufactured via L-PBF and LP-DED processes. It has been reported that the L-PBF CoCr specimens have significantly higher tensile strength and ductility than the LP-DED counterparts. It has been shown that the considerably higher cooling rate of the L-PBF process resulted in a much finer microstructure while compared with those of the LP-DED samples. Several studies have reported various constituent phases in IN718 fabricated via the two AM techniques due to variation in thermal history. The microstructure of the L-PBF IN718 in non-heat treated (NHT) condition is found to be spheroidal/ellipsoidal γ' in γ matrix [9], whereas LP-DED counterparts' is Laves phase in interdendritic γ matrix [10,11]. Likewise, a lamellar α+ß structure has been reported for the L-PBF Ti-6Al-4V [12], while the LP-DED counterparts have fine lamellar Widmanstatten structure along with grain boundary α phase in the coarse columnar prior ß grains [13]. Therefore, it is essential to understand the differences in the microstructure of the part fabricated with various AM techniques such as L-PBF and LP-DED techniques to establish process-structure-property relationships for various material systems.

The 17-4 PH stainless steel (SS) is among the materials adopted for the AM processes and has high corrosion resistance as well as the various combination of strength and ductility depending on the applied heat treatment. However, its microstructure constituents in the NHT condition is still debated. Although Murr et al. [14] reported a martensitic microstructure for the NHT L-PBF 17-4 PH SS, Alnajjar et al. [15] showed evidence of austenite by-passing during solidification of L-PBF 17-4 PH SS due to the high cooling/solidification rate, which results in a ferritic microstructure. It is worth noting that the chemical composition of the 17-4 PH SS powder may have influences on the solidification order and stable phases [16,17]. Since the cooling/solidification rate varies between the L-PBF and LP-DED process, the as-fabricated microstructure of L-PBF 17-4 PH SS might be different than that of the LP-DED counterpart.

This study aims to investigate and compare the microstructure of 17-4 PH SS manufactured by L-PBF and LP-DED methods. The grain structure and phase constituents in the NHT condition are compared for the L-PBF and LP-DED 17-4 PH SS samples. Further, CALPHAD based phase diagrams are generated to guide the design of heat treatments. The microstructure and texture evolution (i.e., crystallographic orientation of the grains) of L-PBF and LP-DED 17-4 PH SS samples are also compared after different heat treatment steps. The results obtained are fundamental to establish the process-structure relationships for the AM 17-4 PH SS.

Experimental Procedures

Material and Fabrication

The 17-4 PH SS samples in this study were fabricated via both L-PBF and LP-DED processes, using Ar-atomized 17-4 PH SS powder. The detailed chemical composition of the 17-4 PH SS powder used in each of the AM processes is listed in **Table 1**.

Table 1. Chemical composition for 17-4 PH SS powder used for fabrication.

		C	Cr	Ni	Cu	Mn	Si	Nb	Mo	N	O	P	S	Nb+Ta	Fe
L-PBF	**(Wt. %)**	0.01	15.80	4.60	3.67	0.51	0.32	0.32	0.21	0.02	0.04	0.035	0.014	0.27	Bal.
LP-DED	**(Wt. %)**	0.01	16.39	4.17	3.32	0.06	0.78	0.27	0.04	0.01	0.02	0.00	0.00	0.27	Bal.

The L-PBF 17-4 PH SS samples were fabricated using an EOS M290 machine with the EOS default process parameters adopted from Ref. [18] under nitrogen shielding gas. The LP-DED samples were fabricated as round bars on a RPM Innovations (RPMI) 557 machine. The parameters were as follows: power of 1070 W, layer height of 0.38 mm, travel speed of 1,016 mm/min and powder feed rate of 15.1 grams/min. The environment was fully inert using Argon for the LP-DED samples.

Phase Diagrams

To guide the choice of an optimal stress relief (SR) temperature, Thermo-Calc. software was used to generate the Ni-Cr binary phase diagram for17-4 PH SS. For this purpose, the TCFE9 thermodynamic database for various types of Fe-based alloys and steels such as stainless steels was employed [19,20]. Besides, to incorporate the influence of all the alloy elements in generating the phase diagram, the Ni_{eq} (Nickle equivalent) and Cr_{eq} (chromium equivalent) were obtained following the Schaeffler equations [21]:

$$Ni_{eq}\,(wt\%)=\%Ni+0.5(\%Mn)+0.3(\%Cu)+25(\%N)+30(\%C) \quad \text{Eq.1}$$

$$Cr_{eq}(wt\%)=\%Cr+2(\%Si)+1.5(\%Mo)+1.75(\%Nb) \quad \text{Eq.2}$$

The Ni_{eq} and Cr_{eq} values were further calculated for the L-PBF to be 7.6 and 16.6wt%, respectively. For the LP-DED 17-4 PH SS the Ni_{eq} and Cr_{eq} values were found to be 6.1 and 17.7wt%, respectively. **Figure 1** shows the binary phase diagram generated by Thermo-Calc. software for the L-PBF and LP-DED samples encountering their corresponding Ni_{eq} and Cr_{eq} values. The Cr amount for the L-PBF and LP-DED samples are indicated on the phase diagrams to predict the phase constituents in various temperatures. According to the phase diagram, the SR heat treatment was carried out at 650 °C for 1 hour for both L-PBF and LP-DED samples. A similar SR procedure has been performed on AM 17-4 PH SS in the literature [22,23]. However, it must be noted that conducting heat treatment at this temperature for longer durations may cause austenite reversion on the lath martensite boundaries, which will remain in the microstructure upon cooling [24].

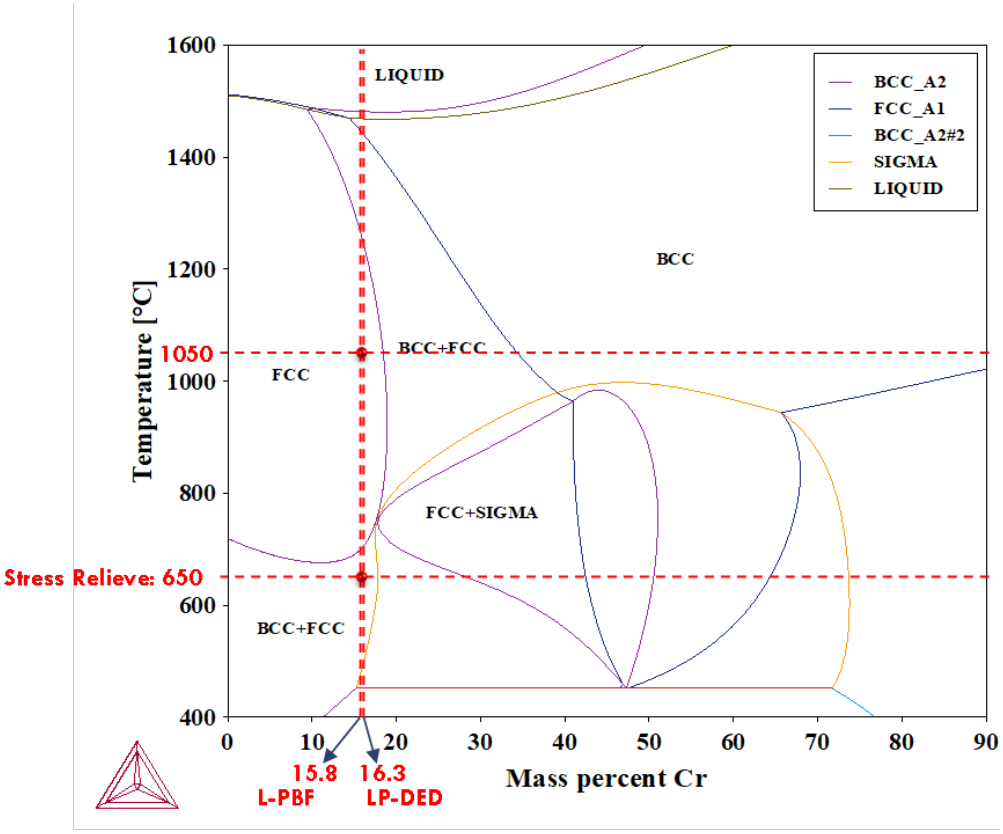

Figure 1. The Ni-Cr binary phase diagram samples generated by Thermo-Calc. software using TCFE9 thermodynamic database [20].

Heat Treatment and Microstructure Characterization

The heat treatment cycles applied on the samples are shown in **Figure 2** schematically. Two sets of heat treatments were conducted; in one set, samples were heat treated directly after fabrication, and for the other set, SR at 650 °C for 1 hour followed by air cooling was carried out prior to conducting the heat treatment. Disk-like samples shown in **Figure 2**(a) were cut in half for a side-by-side comparison between the heat treatment conditions with/without SR. Among the standard heat treatments recommended for wrought 17-4 PH SS, the CA-H1025 heat treatment cycle has been shown to result in both good strength and reasonable ductility as well as high fatigue resistance, and is therefore used in this study. However, the choice of heat treatment is varied upon on the properties needed for the end use application.

The CA (i.e., condition A) annealing step at 1050 °C (1922 F) is shown in phase diagrams (see **Figure 1**) for both the L-PBF and LP-DED 17-4 PH SS to be in the full austenitic region. Samples were air-cooled after the CA step to room temperature and further aged at 552 °C (1025 F) for 4 hours, i.e., CA-H1025. There are debates and efforts made to show the effect of direct aging in AM martensitic SSs such as Maraging steels; however, it is found that solution annealing heat treatment enhances the mechanical properties significantly, which is attributed to a more homogenized microstructure after CA. It has been reported that direct aging at 552 °C for the L-

PBF 17-4 PH SS fabricated under argon shielding gas results in an abnormal fatigue crack growth (FCG) behavior due to the presence of columnar ferrite grains and string δ-ferrite on the grain boundaries [25].

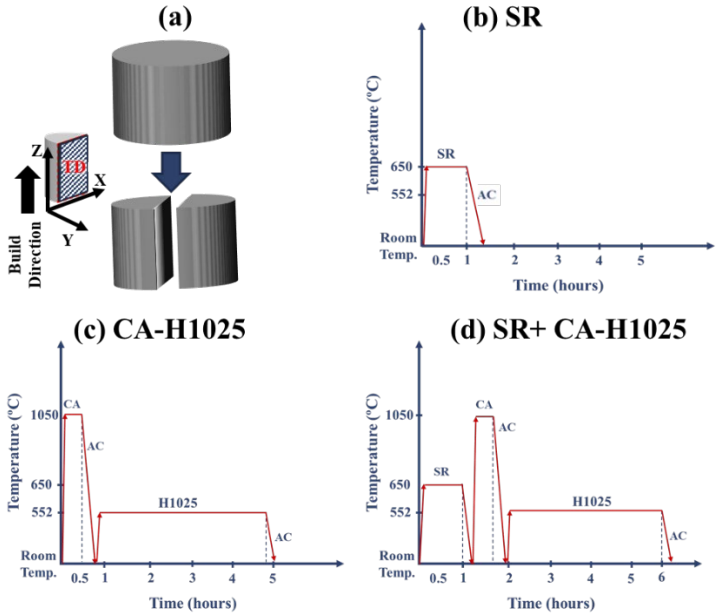

Figure 2. The schematics of (a) the samples for heat treatment and microstructure characterization, and (b)-(d) heat treatment procedures investigated in this study.

The samples were ground and polished using sandpapers with grits 320-4000 following by a mirror-finish polishing step using Chemo-met along with 0.2 µm colloidal silica suspension. The microstructure was further characterized on the plane parallel (X-Z) to the build direction as shown in **Figure 2** using a Zeiss 550 crossbeam scanning electron microscope (SEM) with an electron backscatter diffraction (EBSD) detector. The samples were etched using Braha's reagent to observe the microstructure via SEM. However, for the EBSD analysis as well as electron channeling contrast imaging (ECCI), samples were mirror-finished using a vibratory polisher for 2 hours. The microhardness testing was performed on all the specimens using Anton Par instrument. The force and dwell time for the hardness testing were 100kgf and 5 seconds, respectively.

Results and Discussion

Non-Heat Treated (NHT) Microstructure

The 17-4 PH SS has been reported to have a ferrite-based microstructure while manufactured via AM process in contrast to the precipitated martensitic microstructure in the wrought form. This can be ascribed to the austenite by-passing during fabrication due to the high cooling rate of AM processes [15]. Although the AM processes induce a very high cooling rate naturally, the cooling rate in different AM methods (e.g., L-PBF vs. LP-DED) is not similar. Therefore, the thermal history experienced by the part may be different and result in variation in the microstructure.

The etched microstructure and the ECCI images of L-PBF and LP-DED 17-4 PH SS samples in NHT condition are presented in **Figures 3**(a)&(b) and (c)&(d), respectively. The microstructure of L-PBF 17-4 PH SS is significantly different than that of the LP-DED counterpart. It can be seen in **Figures 3**(a) and (b) that both fine equiaxed and columnar ferrite grains with the lath martensite are present in the L-PBF 17-4 PH SS sample. Normally, the coarse columnar grain structure is seen for most of the AM materials. However, it has been reported that fabricating the L-PBF 17-4 PH SS under nitrogen shielding gas may refine the grain structure and form equiaxed grains as compared to when argon is used as the shielding gas [18]. Therefore, the fine grain structure of the L-PBF 17-4 PH SS sample seen here may be due to the fabrication under nitrogen shielding gas. On the other hand, as presented in **Figures 3**(c) and (d), a coarse columnar ferritic matrix with Widmanstätten ferrite grains is seen in the microstructure of LP-DED 17-4 PH SS sample in NHT condition. The coarse grain structure of the LP-DED 17-4 PH SS sample as compared to that of the L-PBF counterpart is ascribed to the significantly lower cooling rate in the LP-DED process than the L-PBF [3]. In addition, the Cr_{eq}/Ni_{eq} ratio is higher for the LP-DED 17-4 PH SS (~2.9) as compared to that of the L-PBF counterpart (~2.1), which results in higher stability of ferrite in LP-DED sample than L-PBF one.

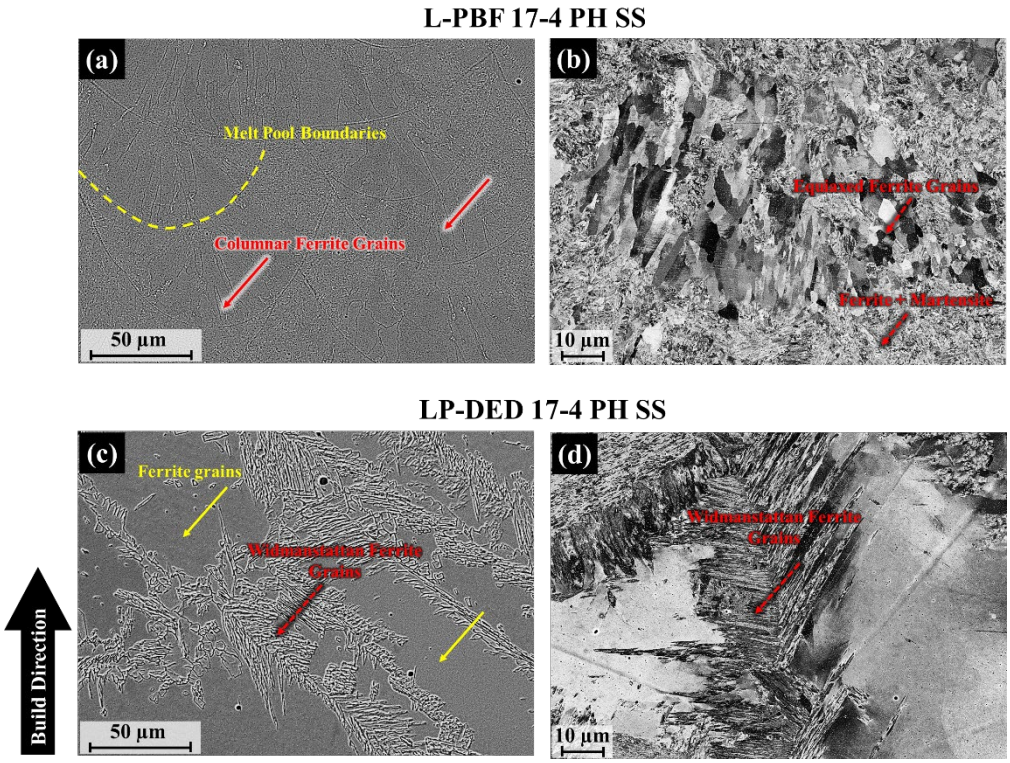

Figure 3. SEM and ECCI micrographs of (a)&(b) L-PBF, and (c)&(d) LP-DED 17-4 PH SS samples.

Heat Treated (HT) Microstructure: Solution annealed + aged

The inverse pole figure (IPF) maps of the L-PBF and LP-DED 17-4 PH SS samples in NHT condition are presented in **Figures 4**(a) and (c), respectively. The EBSD results are taken from the XZ-plane parallel to the build direction as it is schematically illustrated. Note that the colors on the IPF maps represent the crystallographic orientation of the grains. It is seen that the

L-PBF 17-4 PH SS sample (**Figure 4**(a)) has a significantly finer grain structure than that of the LP-DED counterpart (**Figure 4**(c)) in NHT condition, consistent with **Figure 3**. There are grains with size ~1 mm observed in the LP-DED 17-4 PH SS microstructure, although finer grains are also present. These fine grains may have formed surrounding the melt pool boundaries [26]. Considering both the coarse and fine grains, the average grain size for the NHT LP-DED samples is calculated ~93.1 µm. On the other hand, the average grain size for the NHT L-PBF samples is calculated to be ~6 µm.

The microstructures of L-PBF and LP-DED 17-4 PH SS samples after SR heat treatment are shown in **Figures 4**(b) and (d), respectively. As expected, the SR heat treatment conducted on L-PBF and LP-DED 17-4 PH SS samples does not change the grain structure when compared to the NHT condition. The average grain size after SR is calculated ~101.6 µm for the LP-DED samples, and ~5.7 µm for the L-PBF ones, where the variations from the grain size in NHT condition are minimal. In addition, the SR heat treatment applied herein does not change the hardness of the material; the hardness for the NHT L-PBF sample is measured 327±8 HV, while is measured 319±12 HV for the SR L-PBF counterpart. Similarly, the hardness for the NHT LP-DED sample is measured 353±21 HV, while is measured 334±11 HV for the SR LP-DED counterpart.

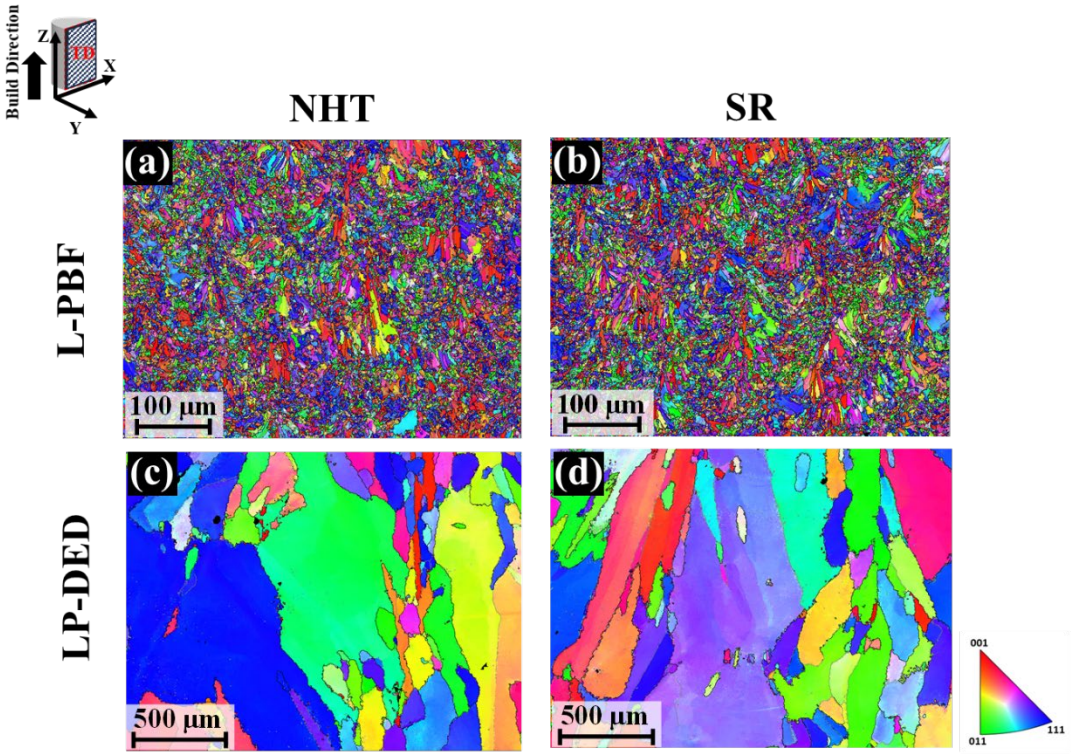

Figure 4. IPF maps of 17-4 PH SS samples in NHT and SR conditions: (a)&(b) L-PBF, and (c)&(d) LP-DED.

It can be seen in **Figure 5**(a) that the ferritic microstructure of L-PBF 17-4 PH SS observed in **Figure 4**(a) transforms to martensitic microstructure after conducting CA-H1025 heat treatment. The phase constituent at 1050 °C (i.e. CA step) is fully austenite (see **Figure 1**), which transforms to martensite after cooling to room temperature as the martensite start temperature (i.e.,

M_s) for the 17-4 PH SS higher than the room temperature (M_s=150 °C) as reported in Ref. [27]. The hardness is increased (415±9 HV) as compared to the NHT condition (327±8 HV) which can be ascribed to the martensitic microstructure and formation of Cu-enriched precipitates. It is worth mentioning that in case there were any δ-ferrite formed during fabrication, it will remain in the microstructure and has been reported to be along with the lath martensite. However, it is postulated that due to using nitrogen as the shielding gas during manufacturing of L-PBF samples, δ-ferrite might not have formed, or at least formed in a very low fraction. It has been well established in the laser welding community that nitrogen decreases the δ-ferrite content in the microstructure of various grades of stainless steels (e.g., 316LN) [28,29]. Conducting SR prior to CA-H1025 (see **Figure 5**(b)) is found to have minimal influence on the phase constituent and grain structure of L-PBF 17-4 PH SS when compared with the sample undergone only CA-H1025 heat treatment condition (**Figure 5**(a)). However, it seems that the SR-CA-H1025 L-PBF sample possesses a slightly finer microstructure than that of the CA-H1025, and the hardness is slightly increased (440±7 HV). The SR heat treatment may have induced recrystallization; therefore, following heat treatment at CA-H1025 after SR resulted in newly formed finer austenite grains, which then formed finer lath martensite as compared to that of CA-H1025 sample.

The microstructure of LP-DED 17-4 PH SS in CA-H1025 (419±14 HV) and SR-CA-H1025 (410±14 HV) heat treatment conditions are presented in **Figures 5**(c) and (d). As seen, the grain structure is more or less similar to that of NHT and SR conditions (see **Figures 3**(b) and (d)) although the hardness increased due to the formation of Cu-enriched precipitates. The fraction of low angle boundaries increased significantly after CA-H1025 heat treatment compared to the NHT condition indicating the formation of subgrains in the larger grains as a result of dislocation rearrangement in the microstructure. This shows that the CA step's temperature and duration (i.e., 1050 °C/0.5 hr) is not sufficient for the LP-DED 17-4 PH SS to recrystallize the grains and result in grain refinement. Comparing the microstructure of L-PBF 17-4 PH SS with that of LP-DED one in CA-H1025 condition, the L-PBF sample has fine lath martensite in fine prior austenite grains (shown by black lines), whereas the ferritic microstructure of the LP-DED sample largely remained. This may be due to the higher Cr_{eq}/Ni_{eq} ratio of LP-DED 17-4 PH SS (~2.9) as well as lower cooling rate in fabrication as compared to the L-PBF process (Cr_{eq}/Ni_{eq}= 2.1), which increases the stability of the ferrite phase in the microstructure of LP-DED 17-4 PH SS samples.

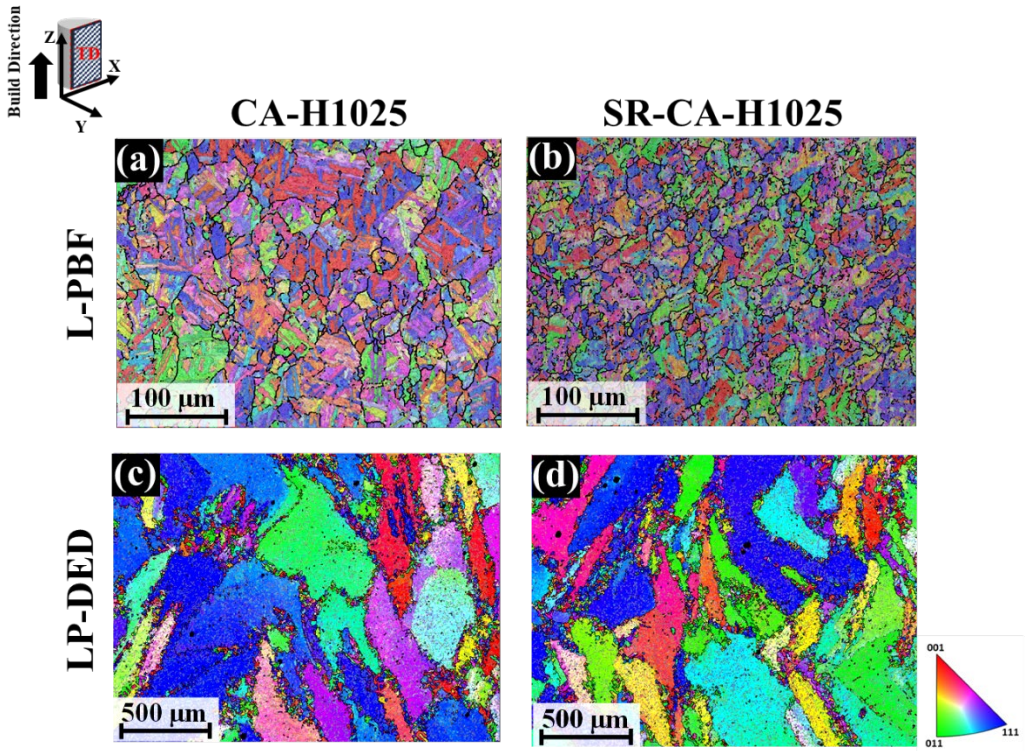

Figure 5. EBSD micrographs of 17-4 PH SS samples undergone CA-H1025 and SR-CA-H1025 heat treatment conditions: (a)&(b) L-PBF, and (c)&(d) LP-DED.

Texture Evolution

The solidification texture for the AM materials is usually reported to be <001> fiber texture, which is the easy growth direction in cubic lattices (i.e., body-centered cubic (BCC), face-centered cubic (FCC)). However, in some cases, the variation in thermal history caused by changing the process parameters (e.g., laser power, scan speed, or build platform preheating, etc.) may alter the crystallographic orientation of the grains [30]. Moreover, the post heat treatment at high temperatures also changes the as-solidified texture due to the formation of new grains/phases [31]. To understand and compare the crystallographic texture of L-PBF and LP-DED 17-4 PH SS samples, their corresponding orientation distribution functions (ODFs) maps for each condition are presented in **Figure 6**. The ODFs represent the frequency distribution of the continuum of orientations in Euler space. The ODFs intensities are indicated as multiple random density (mrd) units. It is worth noting that only a subspace of Euler space ($0 \leq \varphi_1, \Phi, \varphi_2 \leq 90$) is required to represent the entire texture information of cubic materials. The $\varphi_2=45°$ slice of this subspace contained important textures for BCC materials (see **Figure 6**(a)) and is used to analyze the 17-4 PH SS samples in this study.

It can be seen for the NHT L-PBF 17-4 PH SS sample (see **Figure 6**(b)) that there is a strong cube texture with (001)[010] component; however, there are also components of α-fiber and γ-fiber texture present. The SR heat treatment slightly decreases the texture intensity and randomizes the texture; however, slightly intensified the α-fiber texture with (110)[110] components. Comparing the texture of the CA-H1025 sample with that of the NHT condition, the texture components of CA-H1025 resemble those of NHT ones. On the other hand, conducting SR

prior to the CA-H1025 (i.e., SR-CA-H1025) results in a weaker γ-fiber texture than that of the CA-H1025 condition, and the absence of the cube texture component as compared to the CA-H1025 specimen. This may be due to the fact that SR induces the recrystallization of the new grains. The L-PBF 17-4 PH SS shows to have the typical texture of the BCC materials, i.e., γ-fiber (i.e.,{111}<110>) [31]. In the case of LP-DED 17-4 PH SS shown in **Figure 6**(c), there is not a distinct fiber texture present in the NHT condition, and the texture intensity is also very high. This is due to the presence of very large grains in the microstructure (see **Figure 4** and **Figure 5**); therefore, there are not enough grains to show the distributed texture in ODFs. It can be seen that CA-H1025 and SR-CA-H1025 result in γ-fiber texture, and γ-fiber + rotated cube texture (i.e., {001}<011>), respectively. Nonetheless, the γ-fiber texture is apparently the dominant texture component in both L-PBF and LP-DED 17-4 PH SS, which also is the typical texture for the BCC materials.

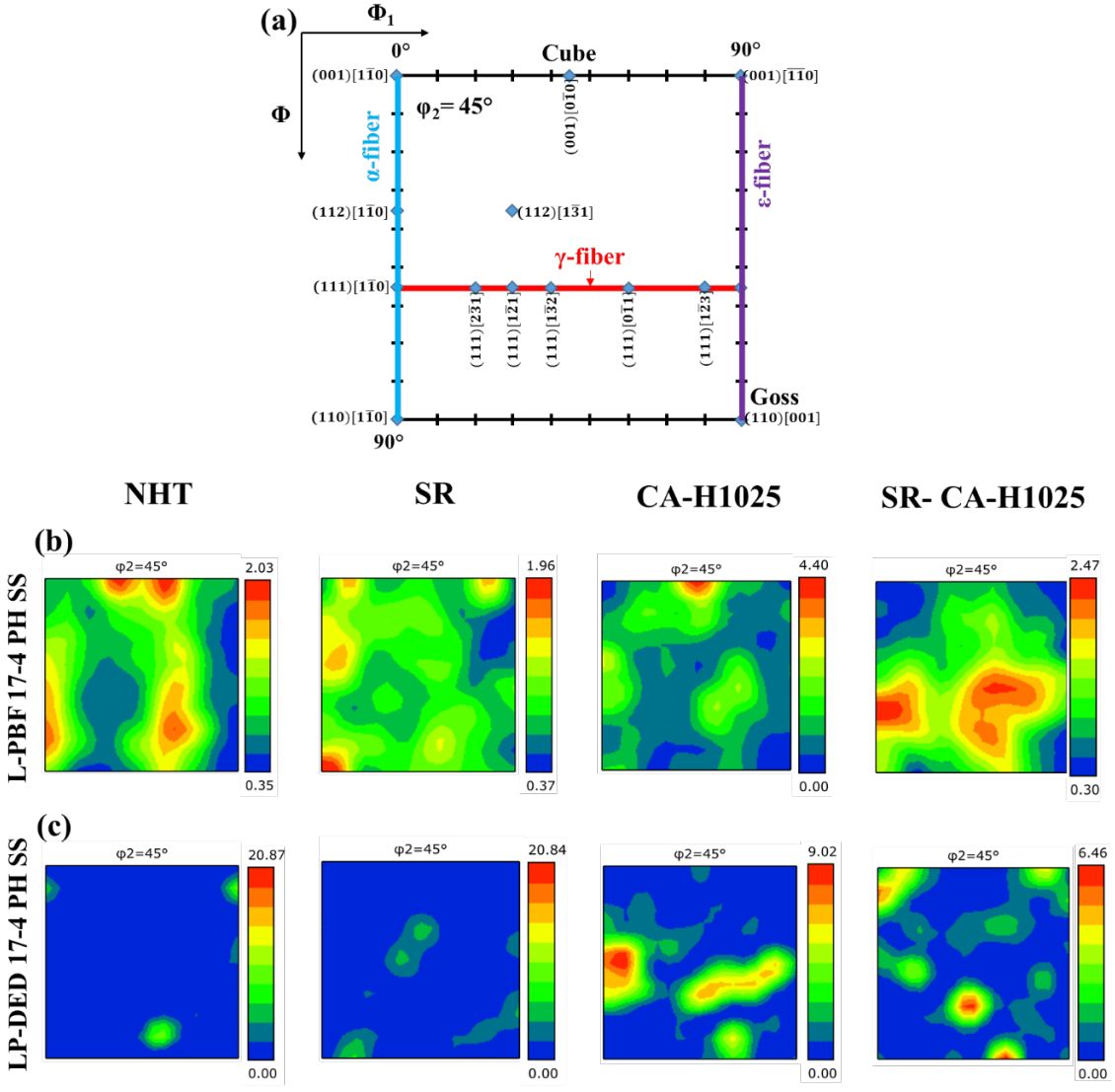

Figure 6. (a) Schematic illustration of the important texture components in BCC materials for $\varphi_2 = 45°$, ODF plots at $\varphi_2 = 45°$ showing texture for (b) L-PBF 17-4 PH SS, and (c) LP-DED 17-4 PH SS after various heat treatments.

Conclusions

This study presented a side-by-side comparison of the microstructure of the L-PBF 17-4 PH SS with that of the LP-DED counterpart in the NHT condition and after heat treatments. SR heat treatment temperature was determined by the chemical compositions of the powders and the Ni-Cr binary phase diagrams. In addition, the texture evolution after heat treatment was also investigated using ODFs. The following conclusions are drawn based on the results presented:

1. The microstructure of the L-PBF 17-4 PH SS sample was composed of fine ferrite grains along with lath martensite, whereas very coarse ferrite grains with the Widmanstätten ferrites along the grain boundaries were observed for the LP-DED 17-4 PH SS sample. This variation in the microstructure was attributed to the lower cooling/solidification rate as well as the higher Cr_{eq}/Ni_{eq} ratio of the LP-DED 17-4 PH SS as compared to the L-PBF one.
2. Using the phase diagram generated by Thermo-Calc., it was found that heat treatment at 650 °C for an hour may be appropriate for the SR heat treatment schedule for both the L-PBF and LP-DED 17-4 PH SS samples. The microstructure and hardness of stress relieved sample were not changed considerably as compared to those of NHT ones.
3. The L-PBF 17-4 PH SS were found to have a cube, partially α- and γ- fiber textures in NHT condition. However, there was no specific texture component characterized for the LP-DED sample in NHT condition based on the EBSD scans performed which can be ascribed to its very large grains.
4. Conducting stress relief (SR) prior to the heat treatment (i.e., SR-CA-H1025) resulted in a less texturized microstructure. This may be due to the effect of SR on inducing recrystallization upon the following heat treatment and result in newly formed grains with random textures.

Acknowledgment

This paper is based upon the work partially funded by the National Aeronautics and Space Administration (NASA) under Award #80MSFC19C0010. Any subjective views or opinions that might be expressed in the paper do not necessarily represent the views of NASA or the United States Government.

References

[1] M. LaMonica, Additive Manufacturing-Innovations, Advances, and Applications, 2013.
[2] T.D. Ngo, A. Kashani, G. Imbalzano, K.T.Q. Nguyen, D. Hui, Additive manufacturing (3D printing): A review of materials, methods, applications and challenges, Compos. Part B Eng. 143 (2018) 172–196.
[3] T.F. Babuska, B.A. Krick, D.F. Susan, A.B. Kustas, Comparison of powder bed fusion and directed energy deposition for tailoring mechanical properties of traditionally brittle alloys, Manuf. Lett. 28 (2021) 30–34.
[4] N. Shamsaei, A. Yadollahi, L. Bian, S.M. Thompson, An overview of Direct Laser Deposition for additive manufacturing; Part II: Mechanical behavior, process parameter optimization and control, Addit. Manuf. 8 (2015) 12–35.

[5] A. Jinoop, C. Paul, K. Bindra, Laser-assisted directed energy deposition of nickel super alloys: A review, Proc. Inst. Mech. Eng. Part L J. Mater. Des. Appl. (2019) 146442071985265.
[6] R. Molaei, A. Fatemi, N. Sanaei, J. Pegues, N. Shamsaei, S. Shao, P. Li, D.H. Warner, N. Phan, Fatigue of additive manufactured Ti-6Al-4V, Part II: The relationship between microstructure, material cyclic properties, and component performance, Int. J. Fatigue. 132 (2020) 105363.
[7] A. Fatemi, R. Molaei, J. Simsiriwong, N. Sanaei, J. Pegues, B. Torries, N. Phan, N. Shamsaei, Fatigue behaviour of additive manufactured materials: An overview of some recent experimental studies on Ti-6Al-4V considering various processing and loading direction effects, Fatigue Fract. Eng. Mater. Struct. 42 (2019) 991–1009.
[8] S.R. Daniewicz, N. Shamsaei, An introduction to the fatigue and fracture behavior of additive manufactured parts, Int. J. Fatigue. 94 (2017) 167.
[9] K.N. Amato, S.M. Gaytan, L.E. Murr, E. Martinez, P.W. Shindo, J. Hernandez, S. Collins, F. Medina, Microstructures and mechanical behavior of Inconel 718 fabricated by selective laser melting, Acta Mater. 60 (2012) 2229–2239.
[10] F. Liu, X. Lin, H. Leng, J. Cao, Q. Liu, C. Huang, W. Huang, Microstructural changes in a laser solid forming Inconel 718 superalloy thin wall in the deposition direction, Opt. Laser Technol. 45 (2013) 330–335.
[11] L.L. Parimi, G. Ravi, D. Clark, M.M. Attallah, Microstructural and texture development in direct laser fabricated IN718, Mater. Charact. 89 (2014) 102–111.
[12] W. Xu, M. Brandt, S. Sun, J. Elambasseril, Q. Liu, K. Latham, K. Xia, M. Qian, Additive manufacturing of strong and ductile Ti–6Al–4V by selective laser melting via in situ martensite decomposition, Acta Mater. 85 (2015) 74–84.
[13] B.E. Carroll, T.A. Palmer, A.M. Beese, Anisotropic tensile behavior of Ti-6Al-4V components fabricated with directed energy deposition additive manufacturing, Acta Mater. 87 (2015) 309–320.
[14] L.E. Murr, E. Martinez, J. Hernandez, S. Collins, K.N. Amato, S.M. Gaytan, P.W. Shindo, Microstructures and properties of 17-4 PH stainless steel fabricated by Selective Laser melting, J. Mater. Res. Technol. 1 (2012) 167–177.
[15] M. Alnajjar, F. Christien, K. Wolski, C. Bosch, Evidence of austenite by-passing in a stainless steel obtained from laser melting additive manufacturing, Addit. Manuf. 25 (2019) 187–195.
[16] P. Sathiya, M.K. Mishra, B. Shanmugarajan, Effect of shielding gases on microstructure and mechanical properties of super austenitic stainless steel by hybrid welding, Mater. Des. 33 (2012) 203–212.
[17] S. Vunnam, A. Saboo, C. Sudbrack, T.L. Starr, Effect of powder chemical composition on the as-built microstructure of 17-4 PH stainless steel processed by selective laser melting, Addit. Manuf. (2019) 100876.
[18] P.D. Nezhadfar, K. Anderson-Wedge, S.R. Daniewicz, N. Phan, S. Shao, N. Shamsaei, Improved high cycle fatigue performance of additively manufactured 17-4 PH stainless steel via in-process refining micro-/defect-structure, Addit. Manuf. 36 (2020) 101604.
[19] S. Cao, Determination of the Fe-Cr-Ni and Fe-Cr-Mo Phase Diagrams at Intermediate Temperatures using a Novel Dual-Anneal Diffusion-Multiple Approach, (2013) 198. https://drive.google.com/open?id=0BwDenrliobpfakx2dTktMWttejg.
[20] T. Software, TCFE9: TCS Steel and Fe-alloys Database, (n.d.).

[21] P.D. Nezhadfar, E. Burford, K. Anderson-Wedge, B. Zhang, S. Shao, S.R. Daniewicz, N. Shamsaei, Fatigue crack growth behavior of additively manufactured 17-4 PH stainless steel: Effects of build orientation and microstructure, Int. J. Fatigue. 123 (2019) 168–179.
[22] H. Irrinki, Material-process-property relationships of 17-4 stainless steel fabricated by laser-powder bed fusion followed by hot isostatic pressing, (2018).
[23] S. Cheruvathur, E.A. Lass, C.E. Campbell, Additive manufacturing of 17-4 PH stainless steel: Post-processing heat treatment to achieve uniform reproducible microstructure, Jom. 68 (2015) 930–942.
[24] P.D. Nezhadfar, R. Shrestha, N. Phan, N. Shamsaei, Fatigue behavior of additively manufactured 17-4 PH stainless steel: Synergistic effects of surface roughness and heat treatment, Int. J. Fatigue. 124 (2019).
[25] P.D. Nezhadfar, E. Burford, K. Anderson-Wedge, B. Zhang, S. Shao, S.R. Daniewicz, N. Shamsaei, Fatigue crack growth behavior of additively manufactured 17-4 PH stainless steel: Effects of build orientation and microstructure, Int. J. Fatigue. 123 (2019).
[26] M. Muhammad, P.D. Nezhadfar, S. Thompson, A. Saharan, N. Phan, N. Shamsaei, A comparative investigation on the microstructure and mechanical properties of additively manufactured aluminum alloys, Int. J. Fatigue. 146 (2021) 106165.
[27] L. Facchini, N. Vicente, I. Lonardelli, E. Magalini, P. Robotti, A. Molinari, Metastable Austenite in 17-4 precipitation-hardening stainless steel produced by selective laser melting, Adv. Eng. Mater. 12 (2010) 184–188.
[28] A.M. Galloway, N.A. McPherson, T.N. Baker, An evaluation of weld metal nitrogen retention and properties in 316LN austenitic stainless steel, Proc. Inst. Mech. Eng. Part L J. Mater. Des. Appl. 225 (2011) 61–69.
[29] R.K. Okagawa, R.D. Dixon, D.L. Olson, The Influence of Nitrogen from Welding on Stainless Steel Weld Metal Microstructures Soluble nitrogen is found to exert a major influence-particularly on the quantity and distribution of weld metal delta ferrite, Weld. Res. Suppl. (1983) 204s-209s.
[30] P.D. Nezhadfar, N. Shamsaei, N. Phan, Enhancing ductility and fatigue strength of additively manufactured metallic materials by preheating the build platform, Fatigue Fract. Eng. Mater. Struct. 44 (2021) 257–270.
[31] L.A.I. Kestens, H. Pirgazi, Texture formation in metal alloys with cubic crystal structures, Mater. Sci. Technol. (United Kingdom). 32 (2016) 1303–1315.